Research Article

High-performance oxygen reduction and evolution carbon catalysis: From mechanistic studies to device integration

John W. F. To[1,§], Jia Wei Desmond Ng[1,2,§], Samira Siahrostami[1,§], Ai Leen Koh[3], Yangjin Lee[4], Zhihua Chen[1], Kara D. Fong[1], Shucheng Chen[1], Jiajun He[5], Won-Gyu Bae[1], Jennifer Wilcox[5], Hu Young Jeong[6], Kwanpyo Kim[4], Felix Studt[7,8,9] (✉), Jens K. Nørskov[1,7] (✉), Thomas F. Jaramillo[1] (✉), and Zhenan Bao[1] (✉)

[1] Department of Chemical Engineering, Stanford University, Stanford, CA 94305, USA

[2] Institute of Chemical and Engineering Sciences, Agency for Science, Technology and Research, Jurong Island 627833, Singapore

[3] Stanford Nano Shared Facilities, Stanford University, Stanford, CA 94305, USA

[4] Department of Physics, Ulsan National Institute of Science and Technology (UNIST), Ulsan 689-798, Republic of Korea

[5] Department of Chemical and Biological Engineering, Colorado School of Mines, Golden, CO 80401, USA

[6] UNIST Central Research Facilities (UCRF), Ulsan National Institute of Science and Technology (UNIST), Ulsan 689-798, Republic of Korea

[7] SUNCAT Center for Interface Science and Catalysis SLAC National Accelerator Laboratory, 2575 Sand Hill Road, Menlo Park, CA 94025, USA

[8] Institute of Catalysis Research and Technology, Karlsruhe Institute of Technology, Hermann-von-Helmholtz Platz 1, 76344 Eggenstein-Leopoldshafen, Germany

[9] Institute for Chemical Technology and Polymer Chemistry, Karlsruhe Institute of Technology, Engesserstr. 18, 76131 Karlsruhe, Germany

[§] These authors contributed equally to this work.

ABSTRACT

The development of high-performance and low-cost oxygen reduction and evolution catalysts that can be easily integrated into existing devices is crucial for the wide deployment of energy storage systems that utilize O_2-H_2O chemistries, such as regenerative fuel cells and metal-air batteries. Herein, we report an NH_3-activated N-doped hierarchical carbon (NHC) catalyst synthesized via a scalable route, and demonstrate its device integration. The NHC catalyst exhibited good performance for both the oxygen reduction reaction (ORR) and the oxygen evolution reaction (OER), as demonstrated by means of electrochemical studies and evaluation when integrated into the oxygen electrode of a regenerative fuel cell. The activities observed for both the ORR and the OER were comparable to those achieved by state-of-the-art Pt and Ir catalysts in alkaline environments. We have further identified the critical role of carbon defects as active sites for electrochemical activity through density functional theory calculations and high-resolution TEM visualization. This work highlights the potential of NHC to replace commercial precious metals in regenerative fuel cells and possibly metal-air batteries for cost-effective storage of intermittent renewable energy.

Address correspondence to Felix Studt, felix.studt@kit.edu; Jens K. Nørskov, norskov@stanford.edu; Thomas F. Jaramillo, jaramillo@stanford.edu; Zhenan Bao, zbao@stanford.edu

1   Introduction

Much research effort has been dedicated to the replacement of fossil fuels with renewable energy sources for the production of electricity [1, 2]. However, due to the intermittent nature of renewable electricity derived from wind or solar power, grid destabilization will become increasingly problematic with its more widespread deployment [3]. Therefore, there is a need to develop cost-effective means to store renewable energy in order to realize a sustainable fossil-fuel-free economy [4]. Regenerative fuel cells (RFCs) represent an interesting class of energy storage devices that are based on H_2-O_2-H_2O chemistries [5]. However, expensive Pt and Ir catalysts are typically required to drive oxygen reduction and water oxidation at an appreciable rate, leading to scalability issues [6]. Thus, the development of high-performance and earth-abundant catalysts that can interconvert O_2 and H_2O with minimal overpotentials remains a critical challenge.

N-doped carbon materials have recently emerged as a promising group of O_2 catalysts owing to their promising activity, low cost, and high degree of tunability in both acidic and alkaline environments [7–11]. Fundamental investigations into these materials have revealed that both the morphology (i.e., the number and size of pores) and the surface functionality (i.e., the abundance and type of heteroatom) play significant roles in their overall O_2 activity [7, 12]. Moreover, defects that are naturally or chemically formed during synthesis can influence the electronic structure of carbon materials and significantly enhance N-doping [13, 14], which is energetically favored to occur near defects [15–17]. This improved understanding has led to marked enhancements in the oxygen reduction reaction (ORR) activity of these materials, some of which now exhibit activities comparable to those of commercial Pt catalysts [12, 18, 19].

There have been fewer studies on these materials for the oxygen evolution reaction (OER) [10, 19–23]. Though carbon materials display high performances in standard three-electrode electrochemical cells, there have been no reports to date on integrating these bifunctional catalysts into operational devices, which is a key step towards replacing the precious metals currently used in RFCs [19, 24]. Furthermore, there is

little information available to guide catalyst design, particularly for the rarer OER carbon catalysts. The development of this kind of high-performance catalyst would enable production of regenerative fuel cell devices.

Herein, we report the preparation of an N-doped hierarchical carbon (NHC) catalyst with rationally designed surface functionality and defect types using a direct soft-templating method followed by a final NH_3 activation step. Compared to the conventional hard-template approach, this NHC synthesis method is facile, cost-effective, and less time consuming [25, 26]. Notably, the catalyst demonstrates high performance for both the ORR and the OER in alkaline environments, achieving an overall O_2 activity that is comparable to that of a commercial Pt/C and Ir/C mixture. By means of density functional theory (DFT) and high-resolution transmission electron microscopy (HR-TEM), we elucidate the design of the catalyst, identifying the active sites for the ORR and OER to be the N-doped defects and carbon defects, respectively. Finally, we demonstrate that these carbon-based materials can be utilized as O_2 catalysts in anion exchange membrane regenerative fuel cells (AEM-RFCs), with the resultant device exhibiting a performance that is comparable to state-of-the-art Pt/Ir AEM-RFCs.

These results suggest that NHC is a high-performance, earth-abundant, and device-compatible bifunctional O_2 catalyst. This work provides new insight into catalyst design, and will contribute towards the replacement of the precious metals typically used for O_2 catalysis in commercial RFCs.

2   Results and discussion

2.1   Catalyst synthesis

The hierarchical porous carbon, which consists of a combination of macropores (ca. 1 μm), mesopores (ca. 5.6 nm) and micropores (< 2 nm), was rationally designed and prepared from a pyrrole monomer precursor. Figure 1 shows a schematic of the synthesis process. We chose a hierarchical morphology because it is beneficial for oxygen reduction catalysis since the mesopores facilitate oxygen diffusion through the catalyst structure while the micropores provide
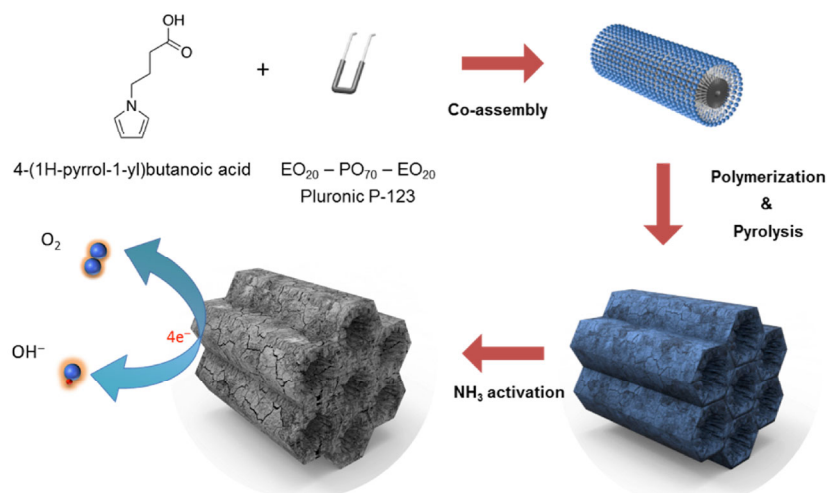
Figure 1 Schematic illustrating the synthesis procedure for NHC. A rationally-designed pyrrole monomer with a hydrophilic anchoring group was synthesized and co-assembled with a triblock copolymer to form a mesophase in an aqueous solution upon polymerization. Carbonization of the polymer co-assembly yields mesoporous carbon with ordered mesopores. Subsequent ammonia activation generates additional micropores to give abundant active sites for electrochemical reactions.

abundant active sites for the reaction [12].

Synthesis of N-doped mesoporous carbon without using a hard template is desirable. Furthermore, polypyrrole was chosen for its high N/C ratio, high pyrolysis yield, and the fact that its aromaticity comprises five-membered heterocyclic rings, which may facilitate the formation of certain defect structures. Consequently, we used the 4-(pyrrol-1-yl)butanoic acid (Py-COOH) monomer, which we have used in previous studies, to provide optimal hydrophilicity for preferential co-assembly with the triblock copolymer surfactant template, and to ensure a fixed position in the palisade region [27, 28]. The mesoporous structure was generated by polymerization of the monomer to give the polymer nanocomposite, followed by carbonization at high temperature under inert gas to remove the low-boiling-point block copolymer template. Unlike in previous work, subsequent activation of the carbonized sample was carried out in ammonia in order to incorporate additional nitrogen content and micropores into the carbon framework. It also induces enhanced N-doping near the pentagonal defects [13, 14, 29].
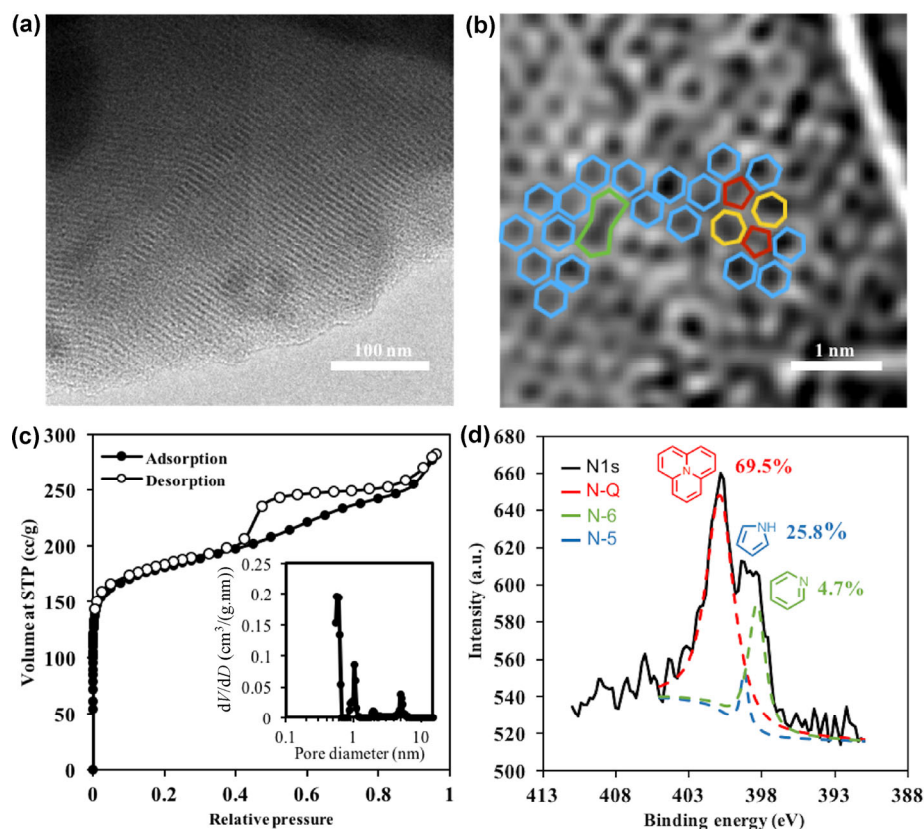
2.2 Physical, structural, and chemical characterization

Scanning electron microscopy (SEM) of the NHC (Fig. S1 in the Electronic Supplementary Material (ESM)) shows the macroporous features of the carbon framework. This catalyst has a granular morphology with a particle size distribution ranging from 100 nm to 5 μm. The TEM image (Fig. 2(a)) reveals a high degree of periodicity when viewed from the [110] direction, indicating a two-dimensional hexagonal mesostructure. HR-TEM imaging was utilized to observe the defect types in a thin region of the carbon sample. As shown in Fig. 2(b) and Fig. S2 (in the ESM), numerous defects, including a Stone–Wales defect and a carbon vacancy, are observed. HR-TEM was also performed on the commercially available mesoporous carbon CMK-3 for comparison, and revealed that it is mainly composed of graphitic carbon, with predominate graphitic fringes and ordered lattices of graphene (Fig. S3 in the ESM).

The porous structure of the NHC catalyst was further analyzed by N_2 adsorption techniques. The nitrogen sorption isotherms (Fig. 2(c)) can be classified as type IV [30]. The steep uptake at low relative pressures reveals the microporous nature ($d < 2$ nm), while the hysteresis at a relative pressure > 0.4 indicates the existence of mesopores, which originate from the removal of the block copolymer template (Fig. 2(c) inset) [31].

The chemical composition of the NHC catalyst is 3.6 wt.% N and 85.3 wt.% C as measured by elemental

Figure 2 Physical, structural, and chemical characterization of NHC. (a) TEM images of NHC showing the [110] direction of the hexagonal array. (b) HR-TEM images of NHC and its respective defect assignments (defects are highlighted for better visualization). (c) Nitrogen adsorption and desorption isotherms at 77 K. The pore size distribution of NHC is shown in the inset. The apparent specific surface area and pore volume of NHC are 573 m²/g and 0.42 cm³/g respectively. A major peak in the cumulative pore volume and pore size distribution scan can be seen at 5.6 nm (d) High-resolution XPS spectra of the N 1s region of NHC. Peak deconvolution reveals the presence of three distinct nitrogen types at 398.5, 400.5, and 401.4 eV, corresponding to pyridinic nitrogen (N-6), pyrrolic nitrogen (N-5), and quaternary nitrogen (N-Q), respectively.

analysis, and 0.5 wt.% Fe as measured by inductively coupled plasma spectrometry (ICP). A small amount of iron residue is detected in the carbon framework due to the use of ferric chloride during the polymerization step that was not completely removed, even after extensive acid washing. However, we observed that increasing the Fe content does not improve the ORR activity.

The nature of the nitrogen species was further investigated by X-ray photoelectron spectroscopy (XPS) in the N1s region as shown in Fig. 2(d). Quaternary nitrogen (N-Q, 401.4 eV) is the most stable nitrogen species under pyrolysis conditions and represents 69% of all nitrogen species [32, 33].

Given these unique features, including small particle size, highly ordered mesopores, considerable microporosity, and abundant nitrogen functionalities, the NHC material exhibits great potential for the ORR.

2.3 ORR activity

The ORR activity of the NHC catalyst in a 0.1 M KOH electrolyte was first studied using a rotating disk electrode (RDE) setup in a three-electrode electrochemical cell. Before NH_3 activation, the catalyst at a 0.28 mg/cm² loading exhibits moderate ORR activity (Fig. 3(a)). This catalyst achieves a half-wave potential—defined as the potential required to reach half of the limiting current—of 0.832 V, and a limiting current density of –4.2 mA/cm². Interestingly, the final NH_3 activation step results in a marked improvement in the ORR activity of the catalyst, with a half-wave potential of 0.882 V and a limiting current density of
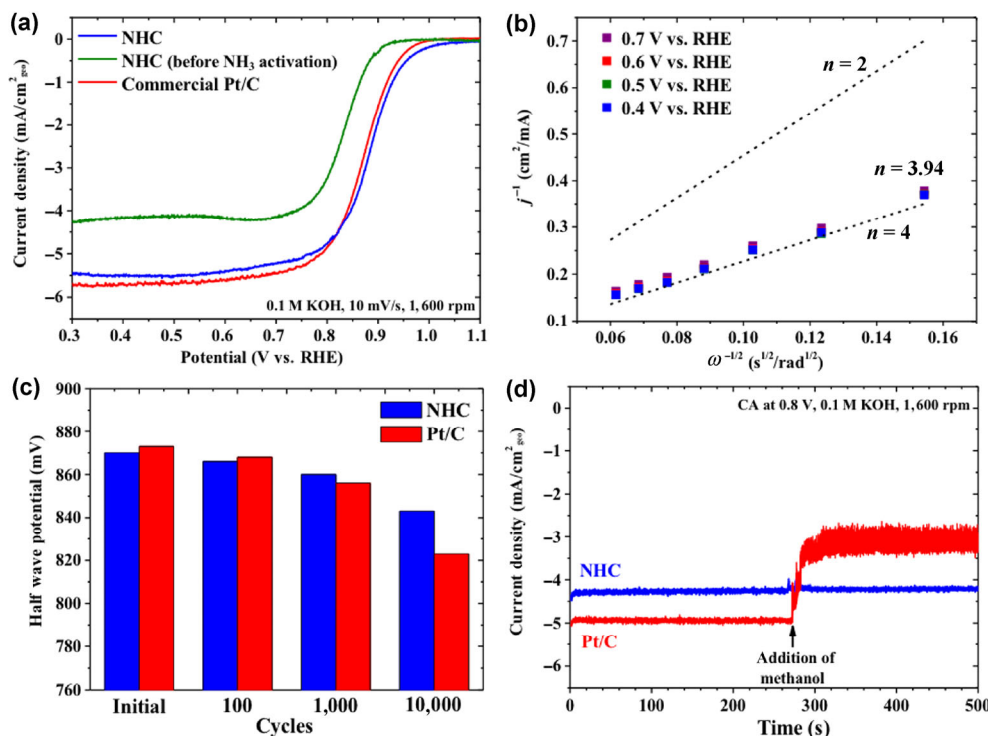
Figure 3 Electrochemical characterization of the ORR performance of NHC. (a) Cyclic voltammograms displaying the ORR activities of NHC before NH_3 activation, NH_3-activated NHC, and a commercial Pt/C for comparison. The voltammograms were obtained in an RDE setup at a rotation rate of 1,600 rpm and a scan rate of 10 mV·s^{-1} in an O_2 saturated 0.1 M KOH electrolyte. (b) Koutecky–Levich plots for four different potentials. The theoretical lines for $n = 2$ and $n = 4$ are shown for comparison. (c) Change in the half wave potentials of NHC and Pt/C after 100, 1,000, and 10,000 cycles of accelerated stress testing. Each cycle involves sweeping the potential between 0.56 and 0.96 V at a 50 mV/s scan rate. (d) Chronoamperometric responses of NHC and Pt/C upon addition of 3 M methanol.

–5.5 mA/cm^2. The enhancement by NH_3 activation can be attributed to a variety of reasons; higher surface area due to the generation of micropores, improved conductivity, and an increase in the amount of N heteroatoms [12, 34, 35]. Cyclic voltammograms conducted in a separate N_2-saturated electrolyte (Fig. S4 in the ESM) confirm that the current generated is due to O_2 reduction. In fact, the half-wave potential achieved by the NHC catalyst is highly competitive with commercial Pt/C nanoparticles at standard 28 $\mu g_{Pt}/cm^2$ or 0.14 $mg_{catalyst}/cm^2$ loadings, and is comparable to the best-reported carbon-based ORR catalysts with comparable loadings (Table S1 in the ESM) [8, 12, 18, 19, 36, 37].

To obtain a better comparison between the intrinsic activity of the NHC and Pt catalysts, we calculated turnover frequency (TOF), defined as the O_2 molecules reacted per second at each active site (details in the ESM). Since the nature of the active site had not been conclusively determined, we calculated two values

for the number of active sites of the NHC catalyst, one by assuming that all surface atoms are equally active (TOF$_{avg}$), which represents a significantly lower value, and the other by assuming that the active sites are the carbons next to nitrogen heteroatoms (TOF$_{C–N}$) based on the DFT calculations shown below. The TOF$_{avg}$ and TOF$_{C–N}$ of the NHC catalyst are 0.006 and 0.159 O_2/s, respectively, revealing the high activity of the NHC catalyst for the ORR (Table S2 in the ESM). For comparison, the TOF of commercial Pt is calculated as 0.132 O_2/s, which is consistent with literature values for Pt in an alkaline environment [38–40]. We note that TOF calculations are rarely performed for carbon-based materials, and as such we limit our comparisons to Pt only.

Further mechanistic analysis by the construction of Koutecky–Levich plots (Fig. 3(b)) and rotating ring disk electrode (RRDE) measurements (Fig. S5(b) in the ESM) reveal that the number of electrons transferred in the ORR (n) is close to 4.0 (Table S3 in the ESM),

which strongly suggests that the NHC catalyst has a strong selectivity for the preferred full four-electron reduction of O_2 to H_2O.

2.4 ORR stability

Stability is another key catalyst performance metric to consider since fuel cells are subjected to harsh working conditions [41]. We performed accelerated durability testing on the NHC catalyst based on a slight modification of a protocol proposed by the U.S. DOE that simulates typical fuel cell operating conditions [42]. The durability tests reveal that the NHC catalyst is stable during the ORR, requiring only an additional 27 mV to reach the initial half-wave potential after 10,000 cycles (Fig. 3(c) and Fig. S6(a) in the ESM). This reasonable stability may be attributed to the minimal amount of H_2O_2 produced during the ORR, as hydroxyl radicals are known to destroy the active sites [34]. Furthermore, the contiguous mesostructured network might restrict the pathways for active site agglomeration and Ostwald ripening [41]. Most importantly, the stability of the NHC catalyst is higher than that of Pt/C, which loses 50 mV of the initial half-wave potential after 10,000 cycles (Fig. 3(c) and Fig. S6(b) in the ESM).

In addition, an ideal catalyst should also display high tolerance to methanol, which may cross over from the anode of direct methanol fuel cells. Methanol tolerance was investigated by adding methanol to the electrolyte with the NHC electrode held at 0.8 V vs. a reversible hydrogen electrode (RHE). The absence of any appreciable change in activity (Fig. 3(d)) suggests that NHC is resistant against methanol contamination, unlike Pt/C, which shows a 40% drop in activity upon methanol addition owing to active site poisoning. The reasonable stability displayed by the NHC catalyst satisfies another key criterion required for an ORR catalyst alternative to high-cost Pt/C.

2.5 OER and overall O_2 performance

Most literature reports on carbon-based electrocatalysts focus more on the ORR than the OER, which is the oxidative half reaction for water electrolysis that can potentially provide a clean pathway for renewable fuel production [43, 44]. Interestingly, the NHC catalyst

also displays reasonable performance for the OER, requiring 1.678 V to reach 10 mA/cm² (Fig. 4(a)) [5]. Importantly, the OER activity of the NHC catalyst is within 29 mV of that for commercial Ir nanoparticles, and is competitive with the best-reported carbon-based OER catalysts (Table S4 in the ESM) [19, 20].

Carbon is known to undergo oxidation at high potentials, which can lead to a rapid loss of active material [45]. The OER stability of NHC was examined by holding the cell at 10 mA/cm² for 1 h (Fig. 4(b)). The NHC displays reasonable stability, requiring only an additional 38 mV overpotential to reach 10 mA/cm², which is comparable to the stability of Ir nanoparticles. Additionally, a portion of the drop in activity is reversible, as seen from the periodic drop in overpotential, which can be attributed to reversible blockage of active sites due to bubble formation on the catalyst surface, and suggests that most of the OER active sites are still present after the stability test. We note that the ORR activity dropped after OER testing (Fig. 4(c)), strongly suggesting that the active sites for the ORR are different from those of the OER, and are possibly oxidized in the high potential window of the OER. To further understand this phenomenon, XPS was used to characterize the material after electrochemical testing. As determined by the relative peak ratio for N 1s using XPS measurement, the surface concentration of nitrogen decreases by 39% with a change in the distribution of the types of nitrogen (Fig. S7 in the ESM). We postulate that during the OER, nitrogen moieties undergo oxidation, leading to the observed change in the nitrogen functional groups [46]. Additional DFT calculations were performed to confirm that pyridinic nitrogen is the most reactive N-type, favoring NO formation (see the ESM). This further suggests that nitrogen-doped sites are responsible for the ORR activity, which is consistent with the findings of a recent study on the ORR active sites in N-doped carbon [16].

With carbon-based catalyst materials, it is important to investigate how much, if any, of the current drawn might be due to carbon oxidation rather than water oxidation. The faradaic efficiency of NHC for the OER was determined using an O_2 probe in a custom-made cell (Fig. S8 in the ESM). A representative measurement is shown in Fig. 4(d), from which the faradaic efficiency was calculated to be close to 100%.
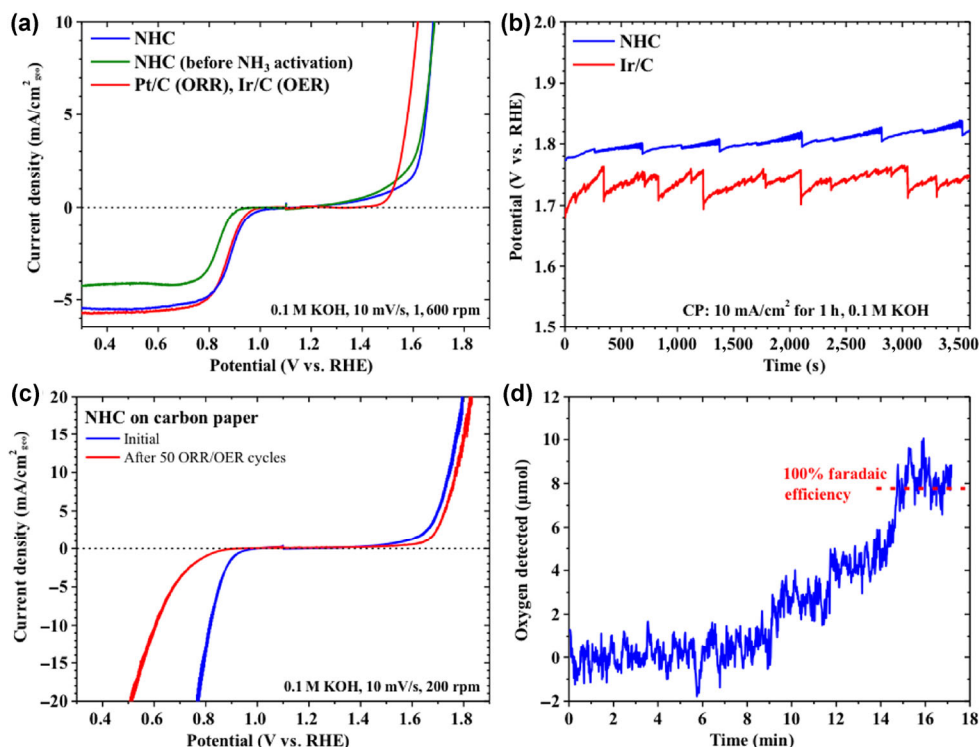
Figure 4 Electrochemical characterization of the OER performance of NHC. (a) Cyclic voltammograms displaying the ORR and OER activities of NHC before NH_3 activation, NH_3-activated NHC, and a precious-metal Pt/C and Ir/C mixture for comparison. (b) Chronopotentiometric responses of NHC and Ir/C held at 10 mA/cm^2 over 1 h. (c) Initial ORR and OER activities of NHC compared to that after 50 ORR/OER cycles. (d) Amount of O_2 detected by the O_2 probe during faradaic efficiency measurements of NHC for the OER. The red dotted line indicates the theoretical amount of O_2 detected given a faradaic efficiency of 100% for 3 C of charge passed at 2 V vs. RHE for 11 min. This data suggests that the majority of the current is due to water oxidation and not to carbon oxidation.

Overall, the RDE testing data verifies that NHC is a high-performance and low-cost bi-functional O_2 catalyst (Fig. 4(a)). Table 1 directly compares the ORR and OER activity of the NHC catalyst and that of a precious-metal based electrode consisting of Pt and Ir. Comparing the overall O_2 activity of the two systems, defined as the voltage difference between that required to drive the OER at 10 mA/cm^2 versus that for the ORR at the half-wave potential (Δ(OER – ORR)),

Table 1 Activity comparison. Comparison of the ORR, OER, and overall oxygen activities of NHC versus a precious-metal Pt/C and Ir/C mixture

Catalyst	ORR (V) (half-wave potential)	OER (V) (potential to reach 10 mA/cm^2)	Δ(OER – ORR) (V)
NHC	0.882	1.678	0.796
Pt/C (ORR) + Ir/C (OER)	0.868	1.619	0.751

reveals that the NHC catalyst is within only 45 mV of the Pt- and Ir-based electrode. This result provides a promising pathway towards replacing precious metals in regenerative fuel cells, and is especially significant given the dearth of bi-functional, carbon-based O_2 catalysts that have been reported.

2.6 Regenerative fuel cell performance

Having developed an active and stable carbon-based ORR-OER bifunctional catalyst, we integrated it into a device environment. There have been limited reports of carbon-based catalysts driving the ORR in an operational anion exchange membrane fuel cell (AEMFC) [19, 24, 47, 48], let alone in an AEM-RFC. Therefore, we examined the performance of NHC in a working device environment by incorporating the catalyst into an AEM-RFC. Two separate membrane electrode assemblies (MEAs) were prepared, one for a fuel cell setup and the other for an electrolyzer setup.

A schematic of the resultant device during operation as a fuel cell and as an electrolyzer is presented in Fig. S11 (in the ESM).
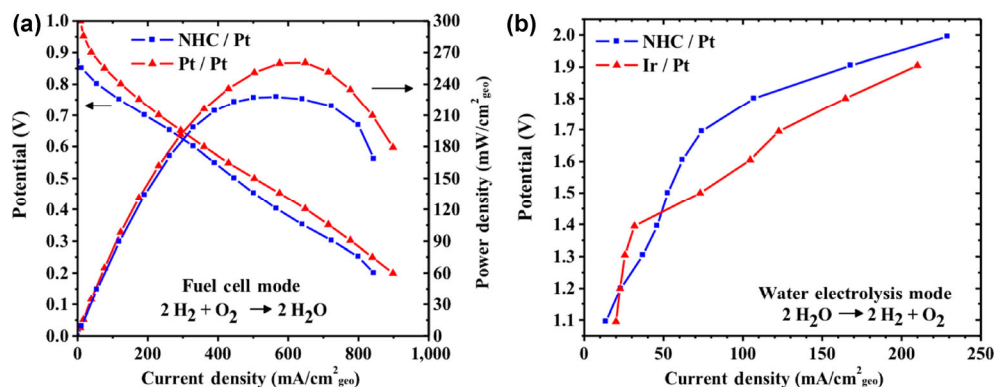
The polarization and power density curves of the NHC/Pt AEM-RFC in fuel cell mode are shown in Fig. 5(a). The peak power density obtained at a cell temperature of 70 °C is 228 mW/cm² at 0.40 V. Notably, this performance is competitive with that of a state-of-the-art Pt/Pt AEMFC, which delivers a peak power density of 260 mW/cm² (Fig. 5(a)). In addition, the performance is superior to those of analogous AEMFCs (carbon-based ORR catalyst, Pt/C hydrogen oxidation reaction (HOR) catalyst) reported (Table S5 in the ESM). Given the low cost of Pt-free catalysts and the mass transport issues arising from a thick catalyst layer, it has been proposed that the figure-of-merit for non-precious catalysts is their volumetric activity at 0.8 V [49]. We determined the volumetric activity of the NHC catalyst at 0.8 V to be 2,600 A/cm³ (see the ESM), which is well beyond the 300 A/cm³ DOE target for 2015, indicating the exciting possibility of using NHC as a cathode fuel cell catalyst [50].

The NHC/Pt AEM-RFC was also tested in water electrolysis mode. Figure 5(b) shows the polarization curve. The cell achieves a current density of 200 mA/cm² at 1.95 V and 70 °C, which is close to the 1.88 V required for our state-of-the-art Ir/Pt AEMEC. Overall, the performance of the NHC/Pt AEM-RFC is close to that of our state-of-the-art precious-metal Pt/Ir AEM-RFC,

and to the best of our knowledge, this is the first report of a semi-precious AEM-RFC (carbon-based OER catalyst, Pt/C hydrogen evolution reaction (HER) catalyst).

2.7   Mechanistic study

To gain further insight into the nature of the active sites for the ORR and OER, we performed DFT calculations on various carbon-based structures with and without nitrogen. The substantial contribution of pentagonal defects to oxygen reduction activity has recently been identified in carbon-based metal-free catalysts [51]. In this work, we considered a wide range of different types of defects (Fig. S13 in the ESM), including single vacancy (SV) and double vacancies (DVs), such as 555-777 (Fig. 6(a), A3), 5555-6-7777 (Fig. 6(a), A4), 555-6-777 (Fig. 6(a), A5 & A6), and Stone–Wales 55-77 (Fig. 6(a), A7) and 585 (Fig. S13 in the ESM) [52] together with their N-doped versions. Here, the 5, 6, and 7 denote the pentagon, hexagon, and heptagon in the defect configuration. Our calculations indicate that SV and 585 DV are too reactive to contribute to oxygen catalysis, while some of the DVs are able to catalyze both the ORR and OER. The active site is located at the pentagons as marked in Fig. 6(a). We show that pentagons in different types of defects represent markedly different activities. We also show that N-doping in the DV defects, which is shown to be energetically favored in the pentagons

Figure 5 Evaluation of NHC performance as a regenerative fuel cell catalyst. (a) Polarization and power density curves for an AEMFC held at 70 °C utilizing NHC as the ORR catalyst and commercial Pt/C as the HOR catalyst. An analogous Pt/Pt AEMFC is shown as a comparison. (b) Polarization curve for an AEMEC held at 70 °C using NHC as the OER catalyst and commercial Pt/C as the HER catalyst. An analogous Ir/Pt AEMFC is shown for comparison purposes. Given that Ir exhibits higher activity for the OER than NHC as shown during RDE tests, it is not unexpected that the Ir/Pt AEMEC exhibits slightly higher performance than that of the NHC/Pt AEMEC.
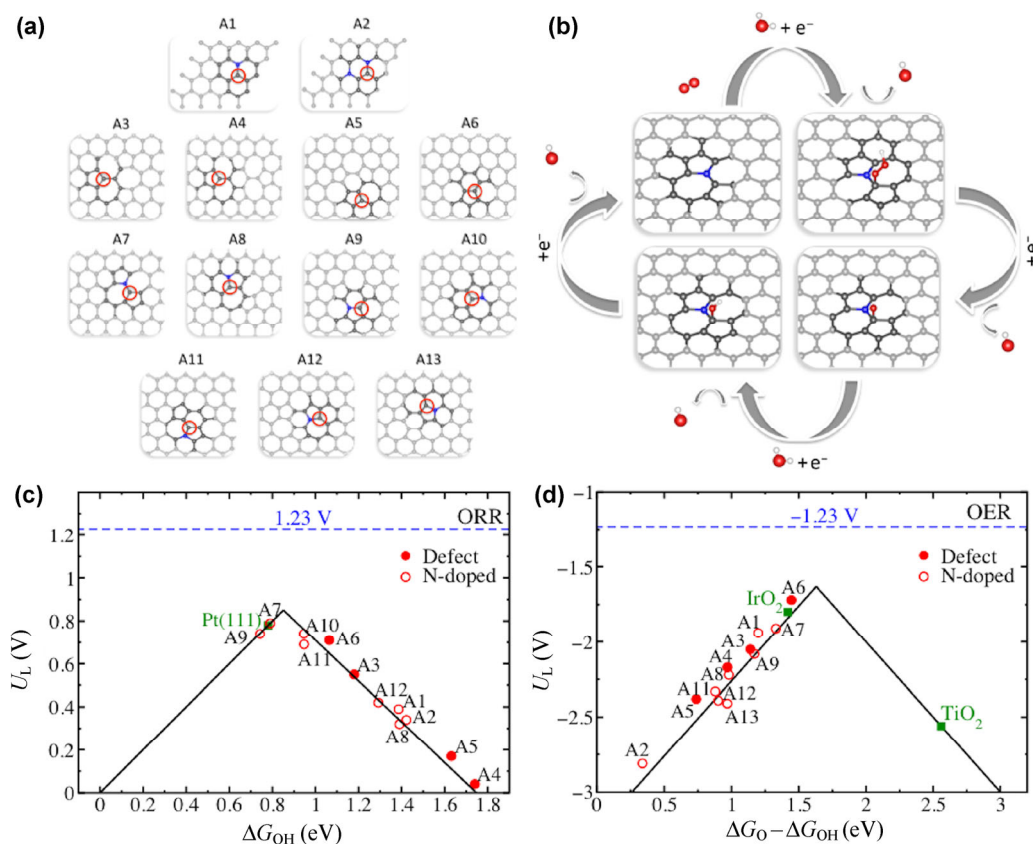
Figure 6 DFT calculations on various carbon-based structures. (a) Examined carbon based materials displayed in the volcano plots. Both volcano plots are based on the RHE scale. For each examined structure, active sites are marked with red circles. Grey and blue spheres display carbon and nitrogen, respectively. (b) Schematic of the four-electron oxygen reduction reaction pathway on the most active defect structure (A7). (c) and (d) Four-electron volcano plots for reduction of O_2 and oxidation of water displayed with the limiting potential plotted as a function of ΔG_{OH} and $\Delta G_O - \Delta G_{OH}$, respectively. The equilibrium potentials for both the ORR and OER are shown as dashed blue lines. Pt(111) data is adapted from Ref. [46]. IrO_2 and TiO_2 data are adapted from Ref. [49]. The equilibrium potential for ORR (1.23 V) is shown by the dashed blue line in (c).

[13, 14], significantly enhances activity. Figure 6(b) displays a schematic of the four-electron oxygen reduction reaction pathway in alkaline media.

The ORR and OER catalytic activities are determined by the binding energies of reaction intermediates (OH*, O*, and OOH*) to the active sites of the catalyst (Fig. 6(a)) [53]. Our calculations indicate scaling relationships between the binding energies of reaction intermediates (see the ESM), which allow us to establish theoretical activity volcanoes for both the ORR and the OER (Figs. 6(c) and 6(d)).

Figure 6(c) displays the theoretical activity volcano for the ORR on the RHE scale. Limiting potentials (i.e., the maximum potential at which all the elementary steps of water formation are downhill in free energy) are shown as a function of ΔG_{OH} [53, 54]. Our DFT

calculations identify highly active structures for the ORR (the estimates of uncertainties of all calculated values are in the ESM). Note that the theoretical limiting potential for the ORR at an N-doped defect-free structure (A1) is 0.39 V, while the N-free DVs such as 555-777 (Fig. 6(a), A3) and 555-6-777 (Fig. 6(a), A6) have high activities with limiting potentials of 0.55 V and 0.71 V, respectively. Depending on the position of the nitrogen, some of the N-doped DVs (Fig. 6(a), A7 and A9) show activities with a limiting potential of 0.79 and 0.74 V. These are similar to those of many known promising catalysts [54–59]. We note that the topmost active structure is the N-doped version of the Stone–Wales defect (Fig. 6(a), A7), which is the most stable (Table S6 in the ESM) and the most frequently found defect type in the mesoporous structures as

observed by HR-TEM. As the mesoporous structures involve a complex multilayer of graphene, we examined the effect of sublayer graphene on the ORR activity of the defect in Fig. 6(a), A7. Our results show that graphene sublayers have a negligible effect on the predicted activity.

Activity trends for the OER are shown in Fig. 6(d). Here, the theoretical limiting potential is plotted as a function of standard free energy of the $\Delta G_O - \Delta G_{OH}$ step [49]. We found that the most active structure for the OER is the N-free defect (Fig. 6(c), A6) with a theoretical overpotential of 0.47 V, which indicates promising activity compared to those of known metal oxide catalysts [60, 61].

To further confirm that defects on the carbon framework are responsible for the OER active sites, we prepared an N-free defective mesoporous carbon based on previous reported literature and subjected it to electrochemical analysis (Fig. S15 in the ESM) [62]. The N-free defect sample shows acceptable activity for the OER; however, it is not active towards the ORR. This observation once again confirms that different types of active sites are responsible for the two oxygen reactions, and it is in agreement with the results of the DFT calculations.

3 Conclusion

Our soft-templating synthesis process produces a high density of ordered mesopores, which facilitate reactant diffusion to active sites. The catalyst synthesis route was specially designed to be facile and scalable for easy catalyst integration into existing device configurations. Based on DFT calculation, significant enhancement in activity can be achieved by N-doping near the DV defects [15]. The concentration of defects can be tuned by controlling the degree of chemical treatment. An enhancement in the ORR activity is provided by the use of a final NH_3 chemical activation step. Based on computational calculations, we assigned the observed ORR activity to the N-doped moieties on the pentagons of DV defects, while the observed OER activity is possibly due to the defective carbon structure. The fundamental electrochemical testing data described herein validates NHC as a high-performance and stable bi-functional O_2 catalyst.

Further incorporation of the NHC as the O_2 catalyst of an AEM-RFC results in a device with high performance comparable to that of a state-of-the-art precious-metal Pt/Ir AEM-RFC, but at a much lower cost. This cost argument is made more compelling given that the catalyst loading on the O_2 side of an RFC is typically higher than that on the H_2 side since sluggish kinetics affect the ORR/OER more than the HOR/HER [49]. Optimization of the MEA components and synthesis procedure could further improve the cell performance [63], making it potentially more attractive for commercial RFC applications. The development work presented herein, from fundamental catalyst understanding to full-scale devices, provides a practical step towards a potentially commercial-level, precious-metal-free RFC as a cost-effective energy storage device to complement intermittent renewable energy.

4 Methods

4.1 Catalyst synthesis

In a typical synthesis, Pluronic P-123 (0.598 g, Aldrich) acting as the soft template, and $FeCl_3$ (1.14 g) acting as the polymerizing agent, were added to a mixture of Millipore water (15 mL) and 12 M HCl (2.5 mL) cooled with an ice water bath. The solution was vigorously mixed for 2 h before 4-(pyrrol-1-yl)butanoic acid (0.45 mL) was added drop-wise. We found previously that a monomer that is too hydrophilic would stay within the aqueous phase and not assemble, while a monomer that is too hydrophobic would occupy the core of micelles of the triblock copolymer. 4-(pyrrol-1-yl)butanoic acid exhibits the ideal hydrophilicity for the co-assembly process. After vigorous stirring for 20 min, the solution was allowed to sit in an ice water bath for 20 h, followed by hydrothermal heating to 100 °C to polymerize the 4-(pyrrol-1-yl)butanoic acid monomers. The hydrothermal product was then filtered and washed with deionized water repeatedly. Carbonization was performed in a tube furnace at a working pressure of ca. 520 Torr under 60 SCCM N_2 (99.999%) flow. The polymer composite was first heated to 350 °C at a ramp rate of 1 °C/min and held for 3 h to slowly decompose the triblock copolymer surfactant, followed by heating to 600 °C

(1 °C/min) and finally to 800 °C (5 °C/min) and held for 2 h. Chemical activation was carried out in a tube furnace at 900 °C under NH_3 flow for 15 min, with the heating and cooling processes conducted in an Ar-saturated environment.

4.2 Physical and chemical characterization

SEM was performed using an FEI Magellan 400 XHR with a 5 kV accelerating voltage and 25 pA beam current. TEM was carried out using a spherical aberration (image) corrected FEI Titan operated at 80 kV. Elemental composition was measured with XPS (PHI 5000 Versaprobe, Al Kα source). Nitrogen sorption experiments were performed using an Autosorb iQ_2 (Quantachrome) low-pressure gas sorption analyzer with 99.999 % N_2 at 77 K. ICP-OES was carried out using a Thermo Scientific ICAP 6300 Duo View Spectrometer. Further details can be found in the ESM.

4.3 Electrochemical characterization

Electrochemical testing was performed in a three-electrode setup utilizing a graphite rod counter electrode and a Ag/AgCl reference electrode in a 0.1 M potassium hydroxide electrolyte. The working electrode was prepared by first mixing 1.0 mg of NHC, 98 μL of ethanol and 2 μL of cation-exchanged Nafion solution. Then, 5.5 μL of the resulting solution was drop-casted onto a glassy carbon disk (Sigradur G HTW Hochtemperatur-Werkstoffe GmbH) to obtain a catalyst loading of 0.28 mg/cm². For comparison, a 20% Pt/C (Etek) electrode with a standard 28 μg$_{Pt}$/cm² loading was also prepared. For the RDE measurements, the shaft was rotated at 1,600 rpm and the potential was cycled between 0.2 and 1.1 V vs. RHE at 10 mV/s. The ORR activity was determined by subtracting the current obtained in a N_2-saturated electrolyte from that obtained in an O_2-saturated electrolyte. Furthermore, multiple 10 mV/s runs were conducted at different rotation rates ranging from 400 to 2,500 rpm for Koutecky–Levich analysis. The potential scale was calibrated to the RHE using a Pt wire (Sigma-Aldrich) as the working electrode in a H_2-saturated electrolyte, and a value of 0.957 V was obtained. RRDE measurements were carried out by sweeping the disk potential between 0.2 and 1.1 V vs. RHE at 10 mV/s while

holding the Pt ring at 1.2 V vs. RHE. The ring collection efficiency was determined to be 0.21 using the reversible $[Fe(CN)_6]^{4-/3-}$ redox couple. Accelerated stability testing on the NHC catalyst was performed by sweeping the potential between 0.6 and 1.0 V vs. RHE at a scan rate of 50 mV/s for 10,000 cycles. A regular 10 mV/s scan between 0.2 and 1.1 V vs. RHE was conducted after 100, 1,000, and 10,000 cycles to ascertain the change in activity over time. The effect of methanol crossover was examined by first holding the working electrode at 0.8 V vs. RHE for around 4.5 min before adding 3 mL of 3 M methanol to the electrolyte.

The OER activity of NHC was determined in a similar fashion to the ORR testing methodology, except that the potential range chosen was between 1.1 and 1.8 V vs. RHE. For comparison, a 20% Ir/C (Etek) electrode with a standard 28 μg$_{Ir}$/cm² loading was also prepared. The OER stability of NHC was examined by holding the working electrode at 10 mV/s for 1 h. Faradaic efficiency measurements were performed in a gas-tight, two-compartment electrochemical cell (Adams and Chittenden Scientific Glassware) equipped with a commercial electrochemical sensor (Unisense Oxygen Microsensor OX500) as shown in Fig. 8. Further details can be found in the ESM.

4.4 Computational details

The simulations were handled using the Atomic Simulation Environment (ASE) software package [64]. The electronic structure calculations were performed using QUANTUM ESPRESSO program package [65]. The electronic wave functions were expanded in plane waves up to a cutoff energy of 500 eV, while the electron density was represented on a grid with an energy cutoff of 5,000 eV. Core electrons were approximated with ultrasoft pseudopotentials [66]. We used the BEEF-vdW exchange-correlation functional [67], which has been shown to accurately describe chemisorption as well as physisorption properties on graphene. Graphene structures were modeled as one layer. A vacuum region of about 20 Å was used to decouple the periodic replicas. For adsorption studies, supercells of lateral sizes 4 × 4 and 8 × 8 were used, and the Brillouin zones were sampled with (6 × 6 × 1) and (4 × 4 × 1) Monkhorst–Pack k-points, respectively. We estimated the uncertainty of the presented DFT

energies through an ensemble of exchange-correlation functionals representing the known computational errors of the BEEF-vdW functional (Table S7 in the ESM), as reported elsewhere [68].

4.5 MEA fabrication and RFC testing

Four separate MEAs were prepared by a conventional catalyst-coated substrate technique, and utilized commercial AEMs (Fumapem FAA-3, Fumatech). The first MEA, for use in a fuel cell setup, consisted of a cathode with 1.0 mg/cm^2 of NHC and an anode with 1.0 mg/cm^2 of Pt/C. Gas diffusion electrodes (GDEs) were synthesized by first mixing 6.8 mg of the NHC catalyst and 26 µL ionomer (Fumion FAA-3, Fumatech) with 0.136 mL of a water-isopropanol (1:4 volume ratio) solvent. The resulting solution was then painted onto carbon paper (5 cm^2, Sigracet 35BC, Ion Power). For the Pt/C electrodes, 6.8 mg of the Pt/C was mixed with 26 µL of ionomer in 0.271 mL of solvent. An AEM was sandwiched between the GDEs and the resulting MEA was loaded into a 5 cm^2 cell assembly (Fuel Cell Technologies, Inc.). The performance of each MEA was examined using a test system (Fuel Cell Technologies, Inc.) at 70 °C with H$_2$ and O$_2$ (99.999%, Praxair) gases flowing at 200 SCCM. Polarization curves were obtained by stepping the voltage from 1.0 to 0.2 V at 50 mV intervals. The second MEA, for use in an electrolyzer setup, consisted of an anode with 2.0 mg/cm^2 NHC and a cathode with 1.0 mg/cm^2 Pt/C. The MEA was made by the same method and then tested in a similar fashion as that described above, except that water instead of H$_2$ and O$_2$ gases was flowed through the cell, and the voltage range used was 1.1 to 2.0 V. Analogous precious-metal Pt/Pt and Ir/Pt MEAs with 1.0 mg/cm^2 catalyst loading were also tested for comparison purposes.

Acknowledgements

Electronic Supplementary Material: Supplementary material (material characterizations, additional electrochemical studies and detailed DFT calculations) is available in the online version of this article at http://dx.doi.org/10.1007/s12274-016-1347-8.

References

[1] Dunn, B.; Kamath, H.; Tarascon, J.-M. Electrical energy storage for the grid: A battery of choices. *Science* **2011**, *334*, 928–935.

[2] Liu, C.; Li, F.; Ma, L. P.; Cheng, H. M. Advanced materials for energy storage. *Adv. Mater.* **2010**, *22*, E28–E62.

[3] Yang, Z. G.; Zhang, J. L.; Kintner-Meyer, M. C. W.; Lu, X. C.; Choi, D.; Lemmon, J. P.; Liu, J. Electrochemical energy storage for green grid. *Chem. Rev.* **2011**, *111*, 3577–3613.

[4] Aricò, A. S.; Bruce, P.; Scrosati, B.; Tarascon, J.-M.; van Schalkwijk, W. Nanostructured materials for advanced energy conversion and storage devices. *Nat. Mater.* **2005**, *4*, 366–377.

[5] Ng, J. W. D.; Gorlin, Y.; Hatsukade, T.; Jaramillo, T. F. A precious-metal-free regenerative fuel cell for storing renewable electricity. *Adv. Energy Mater.* **2013**, *3*, 1545–1550.

[6] Vesborg, P. C. K.; Jaramillo, T. F. Addressing the terawatt challenge: Scalability in the supply of chemical elements for renewable energy. *RSC Adv.* **2012**, *2*, 7933–7947.

[7] Wood, K. N.; O'Hayre, R.; Pylypenko, S. Recent progress on nitrogen/carbon structures designed for use in energy and sustainability applications. *Energy Environ. Sci.* **2014**, *7*, 1212–1249.

[8] Gong, K. P.; Du, F.; Xia, Z. H.; Durstock, M.; Dai, L. M. Nitrogen-doped carbon nanotube arrays with high electrocatalytic activity for oxygen reduction. *Science* **2009**, *323*, 760–764.

[9] Wang, D.-W.; Su, D. S. Heterogeneous nanocarbon materials for oxygen reduction reaction. *Energy Environ. Sci.* **2014**, *7*, 576–591.

[10] Zhang, J. T.; Zhao, Z. H.; Xia, Z. H.; Dai, L. M. A metal-free bifunctional electrocatalyst for oxygen reduction and oxygen evolution reactions. *Nat. Nanotechnol.* **2015**, *10*, 444–452.

[11] Zhou, X. J.; Qiao, J. L.; Yang, L.; Zhang, J. J. A review of graphene-based nanostructural materials for both catalyst supports and metal-free catalysts in PEM fuel cell oxygen reduction reactions. *Adv. Energy Mater.* **2014**, *4*, 1301523.

[12] Liang, H.-W.; Zhuang, X. D.; Brüller, S.; Feng, X. L.; Müllen, K. Hierarchically porous carbons with optimized nitrogen doping as highly active electrocatalysts for oxygen reduction. *Nat. Commun.* **2014**, *5*, 4973.

[13] Guo, B. D.; Liu, Q.; Chen, E. D.; Zhu, H. W.; Fang, L.; Gong, J. R. Controllable N-doping of graphene. *Nano Lett.* **2010**, *10*, 4975–4980.

[14] Lin, Y.-C.; Lin, C.-Y.; Chiu, P.-W. Controllable graphene N-doping with ammonia plasma. *Appl. Phys. Lett.* **2010**, *96*, 133110.

[15] Hou, Z. F.; Wang, X. L.; Ikeda, T.; Terakura, K.; Oshima, M.; Kakimoto, M.-A.; Miyata, S. Interplay between nitrogen dopants and native point defects in graphene. *Phys. Rev. B* **2012**, *85*, 165439.

[16] Guo, D. H.; Shibuya, R.; Akiba, C.; Saji, S.; Kondo, T.; Nakamura, J. Active sites of nitrogen-doped carbon materials for oxygen reduction reaction clarified using model catalysts. *Science* **2016**, *351*, 361–365.

[17] Zhao, Z. H.; Xia, Z. H. Design principles for dual-element-doped carbon nanomaterials as efficient bifunctional catalysts for oxygen reduction and evolution reactions. *ACS Catal.* **2016**, *6*, 1553–1558.

[18] Jin, J. T.; Pan, F. P.; Jiang, L. H.; Fu, X. G.; Liang, A. M.; Wei, Z. Y.; Zhang, J. Y.; Sun, G. Q. Catalyst-free synthesis of crumpled boron and nitrogen Co-doped graphite layers with tunable bond structure for oxygen reduction reaction. *ACS Nano* **2014**, *8*, 3313–3321.

[19] Ranjbar Sahraie, N.; Paraknowitsch, J. P.; Göbel, C.; Thomas, A.; Strasser, P. Noble-metal-free electrocatalysts with enhanced ORR performance by task-specific functionalization of carbon using ionic liquid precursor systems. *J. Am. Chem. Soc.* **2014**, *136*, 14486–14497.

[20] Zhao, Y.; Nakamura, R.; Kamiya, K.; Nakanishi, S.; Hashimoto, K. Nitrogen-doped carbon nanomaterials as non-metal electrocatalysts for water oxidation. *Nat. Commun.* **2013**, *4*, 2390.

[21] Yang, H. B.; Miao, J. W.; Hung, S.-F.; Chen, J. Z.; Tao, H. B.; Wang, X. Z.; Zhang, L. P.; Chen, R.; Gao, J. J.; Chen, H. M. et al. Identification of catalytic sites for oxygen reduction and oxygen evolution in N-doped graphene materials:

Development of highly efficient metal-free bifunctional electrocatalyst. *Sci. Adv.* **2016**, *2*, e1501122.

[22] Ma, T. Y.; Ran, J. R.; Dai, S.; Jaroniec, M.; Qiao, S. Z. Phosphorus-doped graphitic carbon nitrides grown *in situ* on carbon-fiber paper: Flexible and reversible oxygen electrodes. *Angew. Chem., Int. Ed.* **2015**, *54*, 4646–4650.

[23] Li, R.; Wei, Z. D.; Gou, X. L. Nitrogen and phosphorus dual-doped graphene/carbon nanosheets as bifunctional electrocatalysts for oxygen reduction and evolution. *ACS Catal.* **2015**, *5*, 4133–4142.

[24] Kim, O.-H.; Cho, Y.-H.; Chung, D. Y.; Kim, M. J.; Yoo, J. M.; Park, J. E.; Choe, H.; Sung, Y.-E. Facile and gram-scale synthesis of metal-free catalysts: Toward realistic applications for fuel cells. *Sci. Rep.* **2015**, *5*, 8376.

[25] Sevilla, M.; Yu, L. H.; Fellinger, T. P.; Fuertes, A. B.; Titirici, M.-M. Polypyrrole-derived mesoporous nitrogen-doped carbons with intrinsic catalytic activity in the oxygen reduction reaction. *RSC Adv.* **2013**, *3*, 9904–9910.

[26] To, J. W. F.; He, J. J.; Mei, J. G.; Haghpanah, R.; Chen, Z.; Kurosawa, T.; Chen, S. C.; Bae, W.-G.; Pan, L. J.; Tok, J. B.-H. et al. Hierarchical N-doped carbon as CO_2 adsorbent with high CO_2 selectivity from rationally designed polypyrrole precursor. *J. Am. Chem. Soc.* **2016**, *138*, 1001–1009.

[27] Wan, Y.; Shi, Y. F.; Zhao, D. Y. Supramolecular aggregates as templates: Ordered mesoporous polymers and carbons. *Chem. Mater.* **2008**, *20*, 932–945.

[28] Lipic, P. M.; Bates, F. S.; Hillmyer, M. A. Nanostructured thermosets from self-assembled amphiphilic block copolymer/epoxy resin mixtures. *J. Am. Chem. Soc.* **1998**, *120*, 8963–8970.

[29] Zhang, C. H.; Fu, L.; Liu, N.; Liu, M. H.; Wang, Y. Y.; Liu, Z. F. Synthesis of nitrogen-doped graphene using embedded carbon and nitrogen sources. *Adv. Mater.* **2011**, *23*, 1020–1024.

[30] Rouquerol, J.; Avnir, D.; Fairbridge, C. W.; Everett, D. H.; Haynes, J. M.; Pernicone, N.; Ramsay, J. D. F.; Sing, K. S. W.; Unger, K. K. Recommendations for the characterization of porous solids (Technical Report). *Pure Appl. Chem.* **1994**, *66*, 1739–1758.

[31] Meng, Y.; Gu, D.; Zhang, F. Q.; Shi, Y. F.; Yang, H. F.; Li, Z.; Yu, C. Z.; Tu, B.; Zhao, D. Y. Ordered mesoporous polymers and homologous carbon frameworks: Amphiphilic surfactant templating and direct transformation. *Angew. Chem.* **2005**, *117*, 7215–7221.

[32] Zhong, M. J.; Kim, E. K.; McGann, J. P.; Chun, S.-E.; Whitacre, J. F.; Jaroniec, M.; Matyjaszewski, K.; Kowalewski, T. Electrochemically active nitrogen-enriched nanocarbons with well-defined morphology synthesized by pyrolysis of self-assembled block copolymer. *J. Am. Chem. Soc.* **2012**,

134, 14846–14857.

[33] Pels, J. R.; Kapteijn, F.; Moulijn, J. A.; Zhu, Q.; Thomas, K. M. Evolution of nitrogen functionalities in carbonaceous materials during pyrolysis. *Carbon* **1995**, *33*, 1641–1653.

[34] Byon, H. R.; Suntivich, J.; Shao-Horn, Y. Graphene-based non-noble-metal catalysts for oxygen reduction reaction in acid. *Chem. Mater.* **2011**, *23*, 3421–3428.

[35] Zhou, X. J.; Qiao, J. L.; Yang, L.; Zhang, J. J. A review of graphene-based nanostructural materials for both catalyst supports and metal-free catalysts in PEM fuel cell oxygen reduction reactions. *Adv. Energy Mater.* **2014**, *4*, 1301523.

[36] Chung, H. T.; Won, J. H.; Zelenay, P. Active and stable carbon nanotube/nanoparticle composite electrocatalyst for oxygen reduction. *Nat. Commun.* **2013**, *4*, 1922.

[37] Serov, A.; Artyushkova, K.; Atanassov, P. Fe-N-C oxygen reduction fuel cell catalyst derived from carbendazim: Synthesis, structure, and reactivity. *Adv. Energy Mater.* **2014**, *4*, 1301735.

[38] Couturier, G.; Kirk, D. W.; Hyde, P. J.; Srinivasan, S. Electrocatalysis of the hydrogen oxidation and of the oxygen reduction reactions of Pt and some alloys in alkaline medium. *Electrochim. Acta* **1987**, *32*, 995–1005.

[39] Hsueh, K. L.; Gonzalez, E. R.; Srinivasan, S. Electrolyte effects on oxygen reduction kinetics at platinum: A rotating ring-disc electrode analysis. *Electrochim. Acta* **1983**, *28*, 691–697.

[40] Tammeveski, K.; Tenno, T.; Claret, J.; Ferrater, C. Electrochemical reduction of oxygen on thin-film Pt electrodes in 0.1 M KOH. *Electrochim. Acta* **1997**, *42*, 893–897.

[41] Kibsgaard, J.; Gorlin, Y.; Chen, Z. B.; Jaramillo, T. F. Meso-structured platinum thin films: Active and stable electrocatalysts for the oxygen reduction reaction. *J. Am. Chem. Soc.* **2012**, *134*, 7758–7765.

[42] *Fuel Cell Technologies Office Multi-Year Research, Development, and Demonstration Plan. (n. d.)* [Online]. http://energy.gov/eere/fuelcells/downloads/fuel-cell-technologies-office-multi-year-research-development-and-22 (accessed Jan 29, 2016).

[43] Benck, J. D.; Hellstern, T. R.; Kibsgaard, J.; Chakthranont, P.; Jaramillo, T. F. Catalyzing the hydrogen evolution reaction (HER) with molybdenum sulfide nanomaterials. *ACS Catal.* **2014**, *4*, 3957–3971.

[44] Ng, J. W. D.; Hellstern, T. R.; Kibsgaard, J.; Hinckley, A. C.; Benck, J. D.; Jaramillo, T. F. Polymer electrolyte membrane electrolyzers utilizing non-precious mo-based hydrogen evolution catalysts. *ChemSusChem* **2015**, *8*, 3512–3519.

[45] Wen, Z. H.; Ci, S. Q.; Hou, Y.; Chen, J. H. Facile one-pot, one-step synthesis of a carbon nanoarchitecture for an advanced multifunctonal electrocatalyst. *Angew. Chem., Int. Ed.* **2014**, *53*, 6496–6500.

[46] Stöhr, B.; Boehm, H.; Schlögl, R. Enhancement of the catalytic activity of activated carbons in oxidation reactions by thermal treatment with ammonia or hydrogen cyanide and observation of a superoxide species as a possible intermediate. *Carbon* **1991**, *29*, 707–720.

[47] Palaniselvam, T.; Valappil, M. O.; Illathvalappil, R.; Kurungot, S. Nanoporous graphene by quantum dots removal from graphene and its conversion to a potential oxygen reduction electrocatalyst via nitrogen doping. *Energy Environ. Sci.* **2014**, *7*, 1059–1067.

[48] Waki, K.; Wong, R. A.; Oktaviano, H. S.; Fujio, T.; Nagai, T.; Kimoto, K.; Yamada, K. Non-nitrogen doped and non-metal oxygen reduction electrocatalysts based on carbon nanotubes: Mechanism and origin of ORR activity. *Energy Environ. Sci.* **2014**, *7*, 1950–1958.

[49] Gasteiger, H. A.; Kocha, S. S.; Sompalli, B.; Wagner, F. T. Activity benchmarks and requirements for Pt, Pt-alloy, and non-Pt oxygen reduction catalysts for PEMFCs. *Appl. Catal. B: Environ.* **2005**, *56*, 9–35.

[50] Chen, Z. W.; Higgins, D.; Yu, A. P.; Zhang, L.; Zhang, J. J. A review on non-precious metal electrocatalysts for PEM fuel cells. *Energy Environ. Sci.* **2011**, *4*, 3167–3192.

[51] Jiang, Y. F.; Yang, L. J.; Sun, T.; Zhao, J.; Lyu, Z.; Zhuo, O.; Wang, X. Z.; Wu, Q.; Ma, J.; Hu, Z. Significant contribution of intrinsic carbon defects to oxygen reduction activity. *ACS Catal.* **2015**, *5*, 6707–6712.

[52] Kim, Y.; Ihm, J.; Yoon, E.; Lee, G.-D. Dynamics and stability of divacancy defects in graphene. *Phys. Rev. B* **2011**, *84*, 075445.

[53] Nørskov, J. K.; Rossmeisl, J.; Logadottir, A.; Lindqvist, L.; Kitchin, J. R.; Bligaard, T.; Jónsson, H. Origin of the overpotential for oxygen reduction at a fuel-cell cathode. *J. Phys. Chem. B* **2004**, *108*, 17886–17892.

[54] Viswanathan, V.; Hansen, H. A.; Rossmeisl, J.; Nørskov, J. K. Universality in oxygen reduction electrocatalysis on metal surfaces. *ACS Catal.* **2012**, *2*, 1654–1660.

[55] Zhang, J. L.; Vukmirovic, M. B.; Sasaki, K.; Nilekar, A. U.; Mavrikakis, M.; Adzic, R. R. Mixed-metal Pt monolayer electrocatalysts for enhanced oxygen reduction kinetics. *J. Am. Chem. Soc.* **2005**, *127*, 12480–12481.

[56] Strasser, P.; Koh, S.; Anniyev, T.; Greeley, J.; More, K.; Yu, C. F.; Liu, Z. C.; Kaya, S.; Nordlund, D.; Ogasawara, H. et al. Lattice-strain control of the activity in dealloyed core–shell fuel cell catalysts. *Nat. Chem.* **2010**, *2*, 454–460.

[57] Stamenkovic, V. R.; Mun, B. S.; Mayrhofer, K. J. J.; Ross,

P. N.; Markovic, N. M. Effect of surface composition on electronic structure, stability, and electrocatalytic properties of Pt-transition metal alloys: Pt-skin versus Pt-skeleton surfaces. *J. Am. Chem. Soc.* **2006**, *128*, 8813–8819.

[58] Stamenkovic, V. R.; Mun, B. S.; Arenz, M.; Mayrhofer, K. J. J.; Lucas, C. A.; Wang, G. F.; Ross, P. N.; Markovic, N. M. Trends in electrocatalysis on extended and nanoscale Pt-bimetallic alloy surfaces. *Nat. Mater.* **2007**, *6*, 241–247.

[59] Stephens, I. E. L.; Bondarenko, A. S.; Grønbjerg, U.; Rossmeisl, J.; Chorkendorff, I. Understanding the electro-catalysis of oxygen reduction on platinum and its alloys. *Energy Environ. Sci.* **2012**, *5*, 6744–6762.

[60] Landon, J.; Demeter, E.; İnoğlu, N.; Keturakis, C.; Wachs, I. E.; Vasić, R.; Frenkel, A. I.; Kitchin, J. R. Spectroscopic characterization of mixed Fe–Ni oxide electrocatalysts for the oxygen evolution reaction in alkaline electrolytes. *ACS Catal.* **2012**, *2*, 1793–1801.

[61] Man, I. C.; Su, H. Y.; Calle-Vallejo, F.; Hansen, H. A.; Martínez, J. I.; Inoglu, N. G.; Kitchin, J.; Jaramillo, T. F.; Nørskov, J. K.; Rossmeisl, J. Universality in oxygen evolution electrocatalysis on oxide surfaces. *ChemCatChem* **2011**, *3*, 1159–1165.

[62] Liang, C. D.; Dai, S. Synthesis of mesoporous carbon materials via enhanced hydrogen-bonding interaction. *J. Am. Chem. Soc.* **2006**, *128*, 5316–5317.

[63] Ng, J. W. D.; Gorlin, Y.; Nordlund, D.; Jaramillo, T. F. Nanostructured manganese oxide supported onto particulate glassy carbon as an active and stable oxygen reduction catalyst in alkaline-based fuel cells. *J. Electrochem. Soc.* **2014**, *161*, D3105–D3112.

[64] Bahn, S. R.; Jacobsen, K. W. An object-oriented scripting interface to a legacy electronic structure code. *Comput. Sci. Eng.* **2002**, *4*, 56–66.

[65] Giannozzi, P.; Baroni, S.; Bonini, N.; Calandra, M.; Car, R.; Cavazzoni, C.; Ceresoli, D.; Chiarotti, G. L.; Cococcioni, M.; Dabo, I. et al. QUANTUM ESPRESSO: A modular and open-source software project for quantum simulations of materials. *J. Phys.: Condens. Matter* **2009**, *21*, 395502.

[66] Adllan, A. A.; Dal Corso, A. Ultrasoft pseudopotentials and projector augmented-wave data sets: Application to diatomic molecules. *J. Phys.: Condens. Matter* **2011**, *23*, 425501.

[67] Wellendorff, J.; Lundgaard, K. T.; Møgelhøj, A.; Petzold, V.; Landis, D. D.; Nørskov, J. K.; Bligaard, T.; Jacobsen, K. W. Density functionals for surface science: Exchange-correlation model development with Bayesian error estimation. *Phys. Rev. B* **2012**, *85*, 235149.

[68] Medford, A. J.; Wellendorff, J.; Vojvodic, A.; Studt, F.; Abild-Pedersen, F.; Jacobsen, K. W.; Bligaard, T.; Nørskov, J. K. Assessing the reliability of calculated catalytic ammonia synthesis rates. *Science* **2014**, *345*, 197–200.